

1 **Predicting infrasound transmission loss using deep learning**

2 Quentin Brissaud [<https://orcid.org/0000-0001-8189-4699>],¹ Sven
3 Peter Näsholm [<https://orcid.org/0000-0001-9107-4002>],^{1,2} Antoine
4 Turquet [<https://orcid.org/0000-0003-1920-935X>],¹ and Alexis Le Pichon
5 [<https://orcid.org/0000-0001-6531-069X>]³

6 ¹*NORSAR, Gunnar Randers vei 15, Kjeller, Norway*

7 ²*Department of Informatics, University of Oslo, P.O. Box 1080, NO-0316 Oslo,*
8 *Norway*

9 ³*CEA/DAM/DIF, Arpajon, France*

10 (Dated: December 16, 2021)

11 Modelling the spatial distribution of infrasound attenuation (or transmission loss, TL)
12 is key to understanding and interpreting microbarometer data and observations. Such
13 predictions enable the reliable assessment of infrasound source characteristics such as
14 ground pressure levels associated with earthquakes, man-made or volcanic explosion
15 properties, and ocean-generated microbarom wavefields. However, the computational
16 cost inherent in full-waveform modelling tools, such as Parabolic Equation (PE)
17 codes, often prevents the exploration of a large parameter space, i.e., variations in
18 wind models, source frequency, and source location, when deriving reliable estimates
19 of source or atmospheric properties – in particular for real-time and near-real-time
20 applications. Therefore, many studies rely on analytical regression-based heuristic
21 TL equations that neglect complex vertical wind variations and the range-dependent
22 variation in the atmospheric properties. This introduces significant uncertainties in
23 the predicted TL. In the current contribution, we propose a deep learning approach
24 trained on a large set of simulated wavefields generated using PE simulations and
25 realistic atmospheric winds to predict infrasound ground-level amplitudes up to 1000
26 km from a ground-based source. Realistic range dependent atmospheric winds are
27 constructed by combining ERA5, NRLMSISE-00, and HWM-14 atmospheric models,
28 and small-scale gravity-wave perturbations computed using the Gardner model. Given
29 a set of wind profiles as input, our new modelling framework provides a fast (0.05 s
30 runtime) and reliable (~ 5 dB error on average, compared to PE simulations) estimate
31 of the infrasound TL.

32 **1. INTRODUCTION**

33 Surface and subsurface sources (e.g., explosions, microbaroms, earthquakes) excite low-
 34 frequency acoustic waves, i.e., infrasound, that can travel large distances in the Earth's
 35 atmosphere. The refraction and reflection of infrasound waves back to the surface due
 36 to vertical and horizontal gradients of atmospheric winds and temperatures enable their
 37 detection at ground arrays. Because infrasound waves carry information about the source,
 38 they have traditionally been used to retrieve location and yield estimates of nuclear explosions
 39 (*Evers and Haak, 2010*). Recently, the detection and modelling of infrasound phases have
 40 also enabled the inversion of critical seismic source and subsurface parameters such as focal
 41 mechanism (*Shani-Kadmiel et al., 2021*), focal depth (*Averbuch et al., 2020; Lai et al., 2021*),
 42 ground motions (*Hernandez et al., 2018*), or seismic velocity structures (*Brissaud et al.,*
 43 *2021*).

44 Accurately predicting the spatial distribution of infrasound attenuation, i.e., Transmission
 45 Loss (TL), is key to build robust estimates of source and subsurface characteristics. Parabolic
 46 Equations (PE) (*Waxler et al., 2021*) or finite difference codes (*de Groot-Hedlin, 2008;*
 47 *Brissaud et al., 2016*) are typically used to compute accurate estimates of acoustic amplitudes
 48 in realistic wind structures. However, owing to the prohibitive computational cost of full-
 49 waveform numerical modelling tools, most infrasound studies rely on empirical equations
 50 to relate infrasound amplitudes to source parameters. Widely-used regression equations
 51 include models to estimate the explosion yield from peak infrasound amplitudes (e.g., *Golden*
 52 *et al., 2012*) and empirical equations relating pressure at the source and observed infrasound
 53 amplitudes (*Le Pichon et al., 2012*). In particular, the construction of empirical equations
 54 ignores or greatly over-simplify atmospheric wind structures. For instance, in *Le Pichon*
 55 *et al. (2012)*, the authors assume a single range-independent Gaussian stratospheric duct
 56 to optimize their regression model. Yet, vertical and horizontal wind gradients at various
 57 altitudes can drastically affect the TL at the ground (*de Groot-Hedlin et al., 2010*).

58 Empirical models rely on over-simplistic representations of the wind structures because the
 59 mapping between source frequency, atmospheric specifications, and TL is highly nonlinear and
 60 poorly constrained. In order to bridge the gap between computationally expensive numerical
 61 models and over-simplistic empirical equations, supervised Machine-Learning (ML) models
 62 trained over synthetic or recorded datasets can offer an accurate and inexpensive alternative
 63 to existing modelling tools (*Michalopoulou et al., 2021*). Several authors have employed ML
 64 models to predict TL: *Pettit and Wilson (2020)* built a Physics-Informed Neural Network
 65 (PINN) trained over synthetic PE simulation results to predict attenuation maps (along
 66 range and altitude) in the atmospheric boundary layer. PINN consist in updating the cost
 67 function to include physics-based constraints. This model provides an inexpensive alternative
 68 to existing modelling tools but shows low accuracy as it is difficult adjusting the weights
 69 of the physics-informed parameters in the objective function. Additionally, atmospheric
 70 specifications are encoded using only wind profiles, and this approach was not adapted to
 71 long-range propagation. *Hart et al. (2021)* used a fully connected neural network to predict
 72 two-dimensional (2D) attenuation in a turbulent atmosphere from a set of predefined input
 73 parameters describing the turbulent field. This model shows a relatively low error (< 7 dB)
 74 but relies on over-simplified wind models with a set of 13 inputs to describe the velocity field
 75 which are not representative of long-range propagation.

76 Relating wind structures to TLs is key to accurately reproduce full-waveform simulations.
 77 Instead of using pre-defined parameters to describe the wind velocity field, Convolutional-

78 Neural Networks (CNN, *Krizhevsky et al. (2012)*) provide an excellent solution to identify
 79 patterns of interest within input wind models. Such patterns are extracted using a set of
 80 filters described by a number of coefficients that are optimized during the ML training process.
 81 Such network is typically followed by a set of fully-connected network to relate the encoded
 82 information by the CNN and the output. In this contribution we propose a new ML model
 83 trained over synthetic PE simulations to build ground TL in realistic range-dependent wind
 84 models that both shows a low computational cost compared to existing modelling tools, and
 85 high accuracy over long-range propagation.

86 2. BUILDING A TRANSMISSION-LOSS DATASET

87 Building a synthetic TL dataset requires a modelling tool and a set of atmospheric models.
 88 Similar to *Le Pichon et al. (2012)*, we generate TL profiles using the open-source (PE) solver
 89 ePape, provided by the US National Center for Physical Acoustics (NCPA, *Waxler et al.,*
 90 2021). To provide realistic bounds for the atmospheric models, we collect 524 slices of 1000
 91 km up to 80 km altitude from ERA5 re-analysis models, discretized over 137 altitude levels
 92 (*ECMWF, 2018*) with a horizontal resolution of 1 degree. The spatial step of 1 degree
 93 is picked as a trade-off between the resolution to capture ERA5 spatial variability and
 94 the computational time to both download atmospheric models and run simulations. Since
 95 ERA5 models are limited to around 80 km altitude, we use two empirical models to retrieve
 96 atmospheric properties up to 120 km altitude: HWM-14 to obtain zonal and meridional
 97 winds (*Drob et al., 2015*), and NRLMSISE-00 to retrieve temperatures (*Picone et al., 2002*).
 98 ERA5 and HWM-14/NRLMSISE-00 atmospheric models are stitched together using a cubic
 99 interpolation between over the altitude range of 75 to 85 km. Because atmospheric properties
 100 vary with latitude, longitude, and time of the year, ERA5 profiles are uniformly sampled
 101 between latitudes -40 to 70 degrees, longitudes -150 to 165 degrees, and between years
 102 2010 to 2020 (see Fig. 1a).

103 ERA5 models lack resolution to capture fine-scale wind and temperature fluctuations owing
 104 to, e.g., gravity-wave breaking above the troposphere (*Chunchuzov et al., 2015; Chunchuzov*
 105 *and Kulichkov, 2019*). To account for unresolved wind perturbations at higher altitudes,
 106 infrasound studies typically consider the Gardner model to add gravity-wave perturbations
 107 to the original wind profiles (*Gardner et al., 1993*). Therefore, we account for small-scale
 108 perturbations by considering four Gardner realizations for each atmospheric slice (see green
 109 stage in Fig. 2a). Similar to *Norris and Gibson (2002)*, we generate Gardner perturbations
 110 by considering four altitude levels 84, 70, 45, and 21 km, at which we sample standard
 111 deviations uniformly within the range of, respectively, 1–25, 1–18, 1–10, and 1–5 m/s. Finally,
 112 because the direction of propagation within an atmospheric slice, i.e., upwind or downwind
 113 propagation, greatly alters the TLs at the ground, we augment our dataset of atmospheric
 114 models by running simulations in both scenarios by changing the sign of the projected winds
 115 (see yellow stage in Fig. 2a). Our final dataset includes 20960 simulations.

116 The distribution of effective velocity ratios \bar{c}_{eff} computed from our final atmospheric
 117 model dataset for three different altitude regimes, shown in Fig. 1b, is close to a Gaussian
 118 distribution, centred around $\bar{c}_{\text{eff}} = 1$. This indicates that our dataset includes models with
 119 and without strong high-altitude ducts. The distribution of tropospheric effective velocity
 120 ratios is centred at lower values than for higher-altitude layers. This owes to the small
 121 number of occurrences of tropospheric wave ducts in our dataset. In contrast to large vertical
 122 variations of wind velocities, most ERA5 models show small (< 15 m/s) lateral variations of

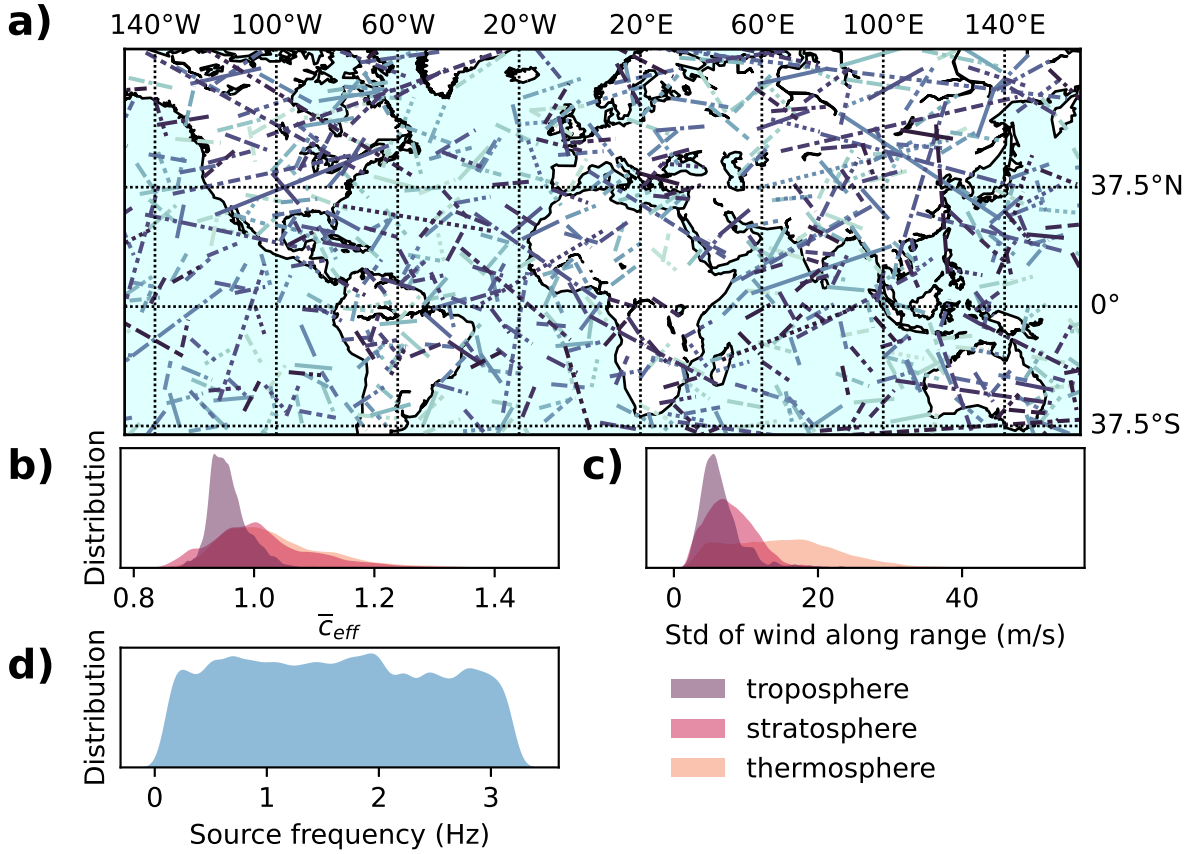


Figure 1. Atmospheric model dataset. (a) distribution of 1000 km long atmospheric slices extracted from the ERA5 dataset. (b) Distribution of effective velocity ratio \bar{c}_{eff} between the ground and various atmospheric layers: troposphere (purple) between 5 and 20 km altitude, troposphere (purple) between 20 and 50 km altitude, and thermosphere (purple) between 50 and 100 km altitude. (c) Distribution of standard deviations of wind velocities along range for various atmospheric layers. (d) Distribution of input source frequencies used in PE simulations to build our TL dataset.

123 wind velocities. The largest lateral wind variations occur above the stratosphere since winds
 124 at these high altitudes are generally the strongest on Earth (*Blanc et al.*, 2018).

125 TL profiles are then computed for a surface sources over 1000 km using 7 Padé coefficients
 126 and the Sutherland-Bass attenuation model (*Sutherland and Bass*, 2004) using NCPA’s ePape
 127 PE simulator (*Waxler et al.*, 2021). Signals from sources of interest (earthquakes, volcanoes,
 128 large explosions) typically show dominant frequencies below 5 Hz. Therefore, similar to
 129 *Le Pichon et al.* (2012), we sample 5 source frequencies from a uniform distribution between
 130 0.1 to 3.2 Hz for each atmospheric slice (see Fig. 1d and Fig. 2a). PE assumes slow lateral
 131 variations in the atmospheric properties over the scale of one wavelength. To ensure smoothly
 132 varying atmospheric properties, we must only consider models that do not include lateral
 133 variations over the scale of the largest wavelength considered, which means $\lambda \approx 3.5$ km at
 134 0.1 Hz. Because we are using a 100 km horizontal sampling, interpolation of atmospheric
 135 properties within the NCPA software will generate smooth-enough models to fulfil the PE
 136 assumptions.

137 PE neglect nonlinear terms and cross winds. Nonlinearities affect primarily the amplitude
 138 and frequency content of thermospheric phases for large-amplitude pressure sources (*Sabatini*
 139 *et al.*, 2019). Therefore, uncertainties on the predicted amplitudes must be accounted for
 140 when investigating high-yield surface sources. When large-amplitude sources are considered,
 141 PE simulations will severally overpredict the amplitude of refracted phases at the ground.
 142 While cross winds have a significant impact on the apparent backazimuth observed from
 143 refracted phases at stations located at large distances from the source, their influence on
 144 infrasound amplitudes is insignificant (*Hernandez et al.*, 2018; *Shani-Kadmiel et al.*, 2021).

145 3. DESIGNING A TRANSMISSION-LOSS MODEL

146 Parabolic equations correspond to a mapping between 2D vertical range-dependent vertical
 147 profiles (temperature, winds, and pressure), frequency, and ground transmission loss profiles
 148 under the effective-velocity approximation (*Waxler et al.*, 2021). Our goal is to find an
 149 alternative nonlinear map between PE inputs and outputs using a neural network in order to
 150 reduce the computational cost. Variations of TL with range for a given source frequency
 151 between different atmospheric models are primarily controlled by lateral and vertical wind
 152 variations. To reduce the complexity of our ML architecture, we simplify the TL-prediction
 153 problem by assuming that there exists an additional nonlinear mapping between frequency,
 154 2D wind variations and TL that approximates the PE solution.

155 Because local wind variations can explain the of infrasound rays back to the surface
 156 (*Chunchuzov et al.*, 2015), we use a Convolutional Neural Network (CNN) to encode the
 157 nonlinear relationship between local wind patterns, represented as 2D images, and TL profiles.
 158 Since the relationship between frequency and TL for complex wind structures is poorly
 159 constrained, we approximate this undefined mapping by using fully-connected layers, which
 160 are the most generic neural network architectures. The final architecture (Fig. 2b) consists
 161 of two layers of 2D convolutions using 5×5 kernels followed by Batch normalization and
 162 Average Pooling. The encoded winds are then concatenated with the source frequency input,
 163 and three fully-connected layers. Average pooling consists of taking the average of the output
 164 of each convolution which is employed to both reduce the dimensionality and learn translation
 165 invariance over the input representation. Batch normalization (*Ioffe and Szegedy*, 2015)
 166 re-centers and re-scale the input of each layer over each mini-batch during the training process.
 167 Normalizing batches reduces the variations of distributions in inputs at each layer, speeds up
 168 training, and produces more reliable models. Both Batch normalization and Average Pooling
 169 layers are used to make the ML model more robust to new data. The last fully connected
 170 layer being the output layer that represents the normalized TL profile between 0 to 1000 km.
 171 All weights are initialized using a uniform Glorot initializer (*Glorot and Bengio*, 2010).

172 To facilitate the recognition of patterns in input data, winds are vertically downscaled and
 173 horizontally upscaled from a 10×1000 2D image, i.e., 10 profiles discretized over 1000 points
 174 along the altitude, to a 50×40 2D images. To limit the range of input and output values,
 175 input profiles and outputs TLs are then normalized by removing the mean and scaled to unit
 176 variance. Both mean and variance are computed over the training dataset only. The output
 177 layer corresponds to the normalized TL profile linearly interpolated it over 500 points within
 178 the range 0 to 1000 km. We train the neural network using an Adam optimizer (*Kingma*
 179 *and Ba*, 2015) with a starting learning rate of 10^{-4} . ReLu activation functions are used
 180 throughout the network expect for the output layer where we do use any activation function.
 181 The ML architecture is implemented in Python using the TensorFlow library (*Abadi et al.*,

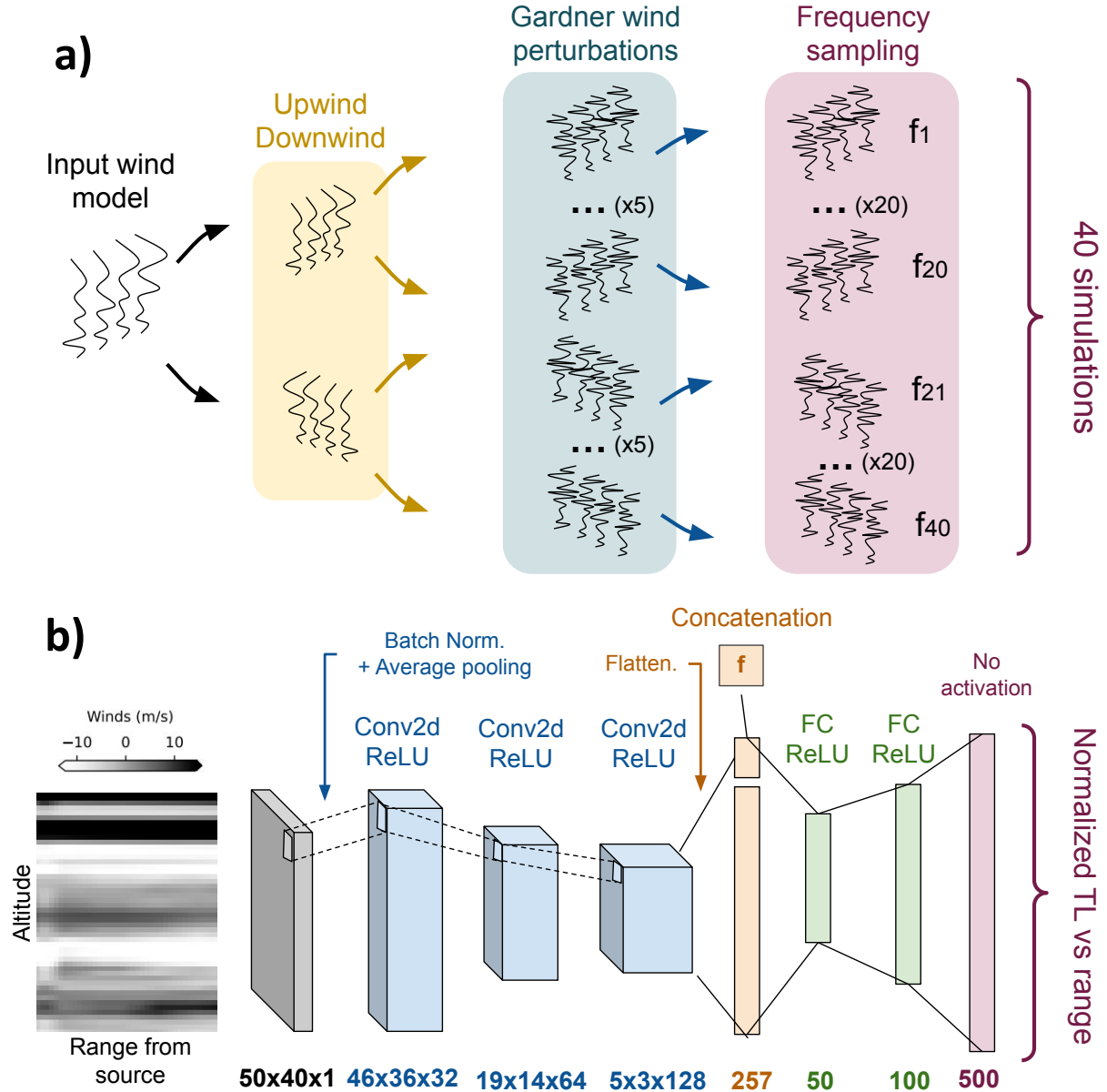


Figure 2. Dataset creation and ML architecture. (a) Procedure to augment our atmospheric model dataset. First upwind and downwind scenarios are considered for each wind slice. The difference between upwind and downwind scenarios corresponds simply to flipping the sign of the projected winds onto the slice. Then, 5 random set of Gardner perturbations are generated for both upwind and downwind scenarios. Finally, 4 input frequencies are considered for each perturbed wind model. A total of 40 wind models are generated for each atmospheric slice extracted from the ERA5 dataset. (b) Cartoon depicting a deep learning network workflow for TL predictions. We use 2D representation of wind amplitudes (grey) with size 50×40 as inputs for our ML model. In the first stage (blue) we use three Convolutional Neural Networks (CNN) to encode the wind information as a vector of size 256. In the second stage (orange), we concatenate this wind encoding with the input source frequency. In the third stage (green), we build a mapping between input frequency and encoded wind representation using two Fully-Connected (FC) layers to finally produce a normalized TL vs range of size 500 (red). This normalized TL can be transformed back to dB by using the scaling transformer used for pre-processing the data.

182 2015). More details about architecture optimization are provided in Appendix A.

183 4. VALIDATION OF MACHINE-LEARNING PREDICTIONS

184 To optimize our ML model, we split our full dataset between 85% training data and 15%
 185 validation data. Strong correlations in TL are expected between PE simulations using wind
 186 models corresponding to perturbed versions of the same original unperturbed wind model
 187 along a given atmospheric slice. Therefore, before training, all simulations corresponding to
 188 the same original atmospheric slice (see the first stage in Fig. 2a) are added to same set (either
 189 training or validation) to make our model more robust to new data. To facilitate convergence,
 190 we adaptatively update the learning rate when the Root Mean-Square-Error (RMSE) does
 191 not decrease over the course of 3 epochs, i.e., training steps. To avoid over-fitting the training
 192 data, we use early stopping if the MSE does not decrease over the course of 12 epochs. Finally,
 193 to speed up the training process, we use mini-batches of size 32.

194 Our ML model converges within 80 epochs with a validation RMSE (over normalized TL
 195 profiles) twice larger than the training RMSE (see Fig. 3a). Once trained, the ML model
 196 has a computational cost of around 0.05 s (Dell T5610 Intel Xeon E5-2630 v2 2.6 GHz 6
 197 CPUs 64GB RAM on CentOS 7) for all input frequencies while PE simulation cost increases
 198 significantly with frequency up to 100 s at 3.2 Hz (see Fig. 3b), which is 2000 times larger
 199 than the cost for a ML prediction at the same frequency. In Figs 3c and 3d, we show that
 200 the RMSE of our ML model follows a bell-shaped distribution centred between 5 to 9 dB
 201 with both variations in distance from the source and source frequency. This distribution
 202 of errors indicates that our ML implementation is stable for the range of frequencies and
 203 distances considered in our dataset. Larger errors tend to occur for high frequencies (> 2
 204 Hz) and close to the source (< 200 km). Higher frequencies are more sensitive to small-scale
 205 wind variations which leads to more complex distributions of TL with range. This added
 206 complexity in high-frequency TMs leads to larger errors in ML predictions. Most TL variations
 207 occur within 200 km from the source with the presence of the first acoustic shadow zone and
 208 first stratospheric return which explains the larger errors observed close to the source.

209 We observe in Figs 3e and 3f that ML predictions match well the average variations of TL
 210 with range from the source. In particular, the ML model captures accurately the TL gain
 211 associated with the different stratospheric returns and the TL asymptotic behaviour at large
 212 distances from the source. However, the ML model does not fully reproduce high-frequency
 213 TL variations, which correspond to small-scale changes in effective wind velocities. The
 214 ML model therefore provides a low-passed solution of the true TL profile. Our model is
 215 unable to learn all small-scale perturbations in the wind models primarily due to the lack
 216 of training data. Yet, small-scale wind perturbations are generally unresolved in currently
 217 available atmospheric models. Therefore, these high-frequency TL perturbations fall within
 218 the uncertainty range associated with available atmospheric model resolutions. Along with
 219 ML predictions, we can determine an estimate of the ML uncertainty u by computing the
 220 median TL error vs range in a given frequency range \mathbf{f} , as the median TL error vs range from
 221 the source over the testing dataset such that $u(r, \mathbf{f}) = \text{median}\{|PE(r, f) - ML(r, f)|\}$, where
 222 r is the range, f is the frequency, PE is the TL predicted using Parabolic Equations, and ML
 223 is the TL predicted using Machine Learning. The frequency dependence of the uncertainty
 224 curves u (see frequency dependence of the errors in Fig 3c) is accounted for by computing the
 225 errors in five frequency ranges \mathbf{f} equally distributed between 0.1 to 3.2 Hz. We observe that
 226 errors between our ML predictions and the PE simulations fall within the ML uncertainty

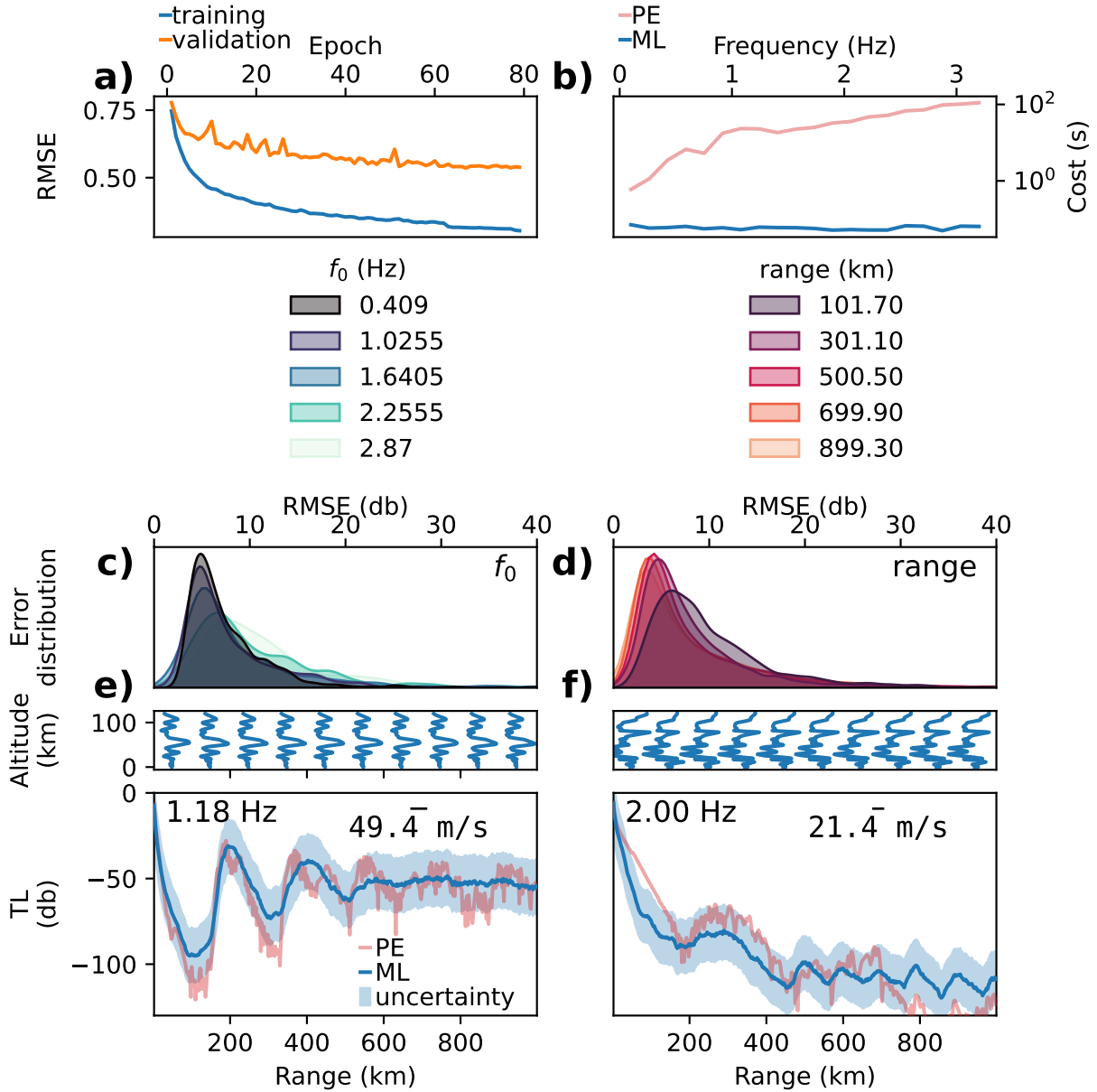


Figure 3. Training and validation of the ML model. (a) Evolution of Root-Mean Square Errors (RMSE) with training epoch. (b) Computational cost of PE simulations (red) and ML predictions (blue) vs input source frequencies. (c) Distribution of RMSE over the testing dataset for various input frequencies. (d) Distribution of RMSE over the testing dataset for various ranges from the source. (e,f) bottom, TL predicted by PE simulations (red) and ML model (blue) along with the ML uncertainty (light blue) for an (e) upwind and (f) downwind wind scenario. (e,f) top, corresponding wind models used for ML predictions. The ML uncertainty u is computed, in a given frequency range \mathbf{f} , as the median TL error vs range from the source over the testing dataset such that $u(r, \mathbf{f}) = \text{median}\{|\text{PE}(r, \mathbf{f}) - \text{ML}(r, \mathbf{f})|\}$, where r is the range, \mathbf{f} is the frequency, PE is the TL predicted using Parabolic Equations, and ML is the TL predicted using Machine Learning.

227 range (blue shaded region in Figs 3e and 3f). As suggested by the distributions showed in
 228 Figs 3c and 3d, the uncertainty range remains stable with variations in frequency and range
 229 from the source.

230 Transfer Learning (TrLe) is typically used to improve the performances of CNNs over
 231 small datasets. Here, TrLe consists of using a CNN network pre-trained over a large dataset
 232 of 2D images for a different task (e.g., multi-class classification of real images from a dataset
 233 such as ImageNet *Deng et al. (2009)*) to initialize our wind encoding stage. This technique
 234 assumes that there are some invariances between our wind-encoding problem and traditional
 235 image-segmentation problems. We tested TrLe by replacing our CNN encoding stage (blue
 236 in Fig. 2b) by both a VGG16 (*Simonyan and Zisserman, 2015*) or a ResNet50 (*He et al.,*
 237 *2016*) network and trained our network using their pre-trained weights and removing pooling
 238 layers. However, TrLe’s performances were worse (RMSE = 9) than with the model presented
 239 in Fig. 2b owing to the significant differences between both the set of images used for training
 240 in VGG16 or ResNet50 and our wind inputs and the problem of image detection vs TL
 241 prediction. .

242 5. ANALYTICAL VS ML PREDICTIONS OF GROUND TLS

243 Stratospheric winds are one of the dominant factors to explain the refraction of acoustic
 244 waves at large distances from the source (*de Groot-Hedlin et al., 2010*). A widely used
 245 empirical regression equation, introduced in *Le Pichon et al. (2012)*, referred in the rest of the
 246 paper as LP12, has provided estimates of TL over large distances from a variety of surface
 247 sources (*Hernandez et al., 2018; Vorobeva et al., 2020; De Carlo et al., 2021*). However,
 248 the original model was optimized over a set of idealized synthetic and range-independent
 249 models where the main feature was a stratospheric duct of various strength, modelled using
 250 a Gaussian wind profile centered at 50 km altitude added to the U.S. Standard Atmosphere.

251 Estimates of LP12 uncertainties over idealized range-independent profiles (*Tailpied et al.,*
 252 *2021*) show low errors compared to PE simulations (< 10 dB) when strong winds are ducting
 253 the signal in the stratosphere. However, in the case of upwind propagation, the accuracy
 254 decreases significantly, especially at high frequencies where the errors can be up to 70 dB.
 255 Yet, uncertainties introduced by this empirical model for realistic range-dependent wind
 256 models are still mostly unconstrained. Comparisons with our PE simulation dataset offer
 257 the opportunity to investigate the uncertainties associated with highly heterogeneous wind
 258 models for both LP12 and our ML model.

259 A typical approach to investigate the influence of stratospheric winds on refracted infra-
 260 sound is to represent the variations of TLs with variations in stratospheric effective velocity
 261 ratios, i.e., stratospheric wind strength, and range from the source for different frequencies
 262 (*Le Pichon et al., 2012*). Yet, in contrast to the dataset used for the optimization of LP12,
 263 effective velocity ratios in our dataset are not equally distributed since we use the atmospheric
 264 model products and not idealized profiles. To provide meaningful comparisons with LP12,
 265 we build uniformly-spaced 2D TL maps by performing a linear interpolation of the ML-
 266 and PE-predicted TLs between $0.8 \leq \bar{c}_{\text{eff}, 40-50 \text{ km}} \leq 1.2$, where $\bar{c}_{\text{eff}, 40-50 \text{ km}}$ is the effective
 267 velocity ratio between 40 to 50 km altitude. Linearly-interpolated TL maps are shown in
 268 Fig. 4. Comparison between Figs 4a and 4b as well as between Figs 4e and 4f shows that
 269 the PE-based TL is well-reproduced by ML over the range of frequencies considered. As
 270 mentioned earlier, our ML model tends to smooth out the rapid oscillations in TL predicted
 271 by PE simulations. Yet, average errors shown in Figs 4d and 4h are stable around 5 dB for

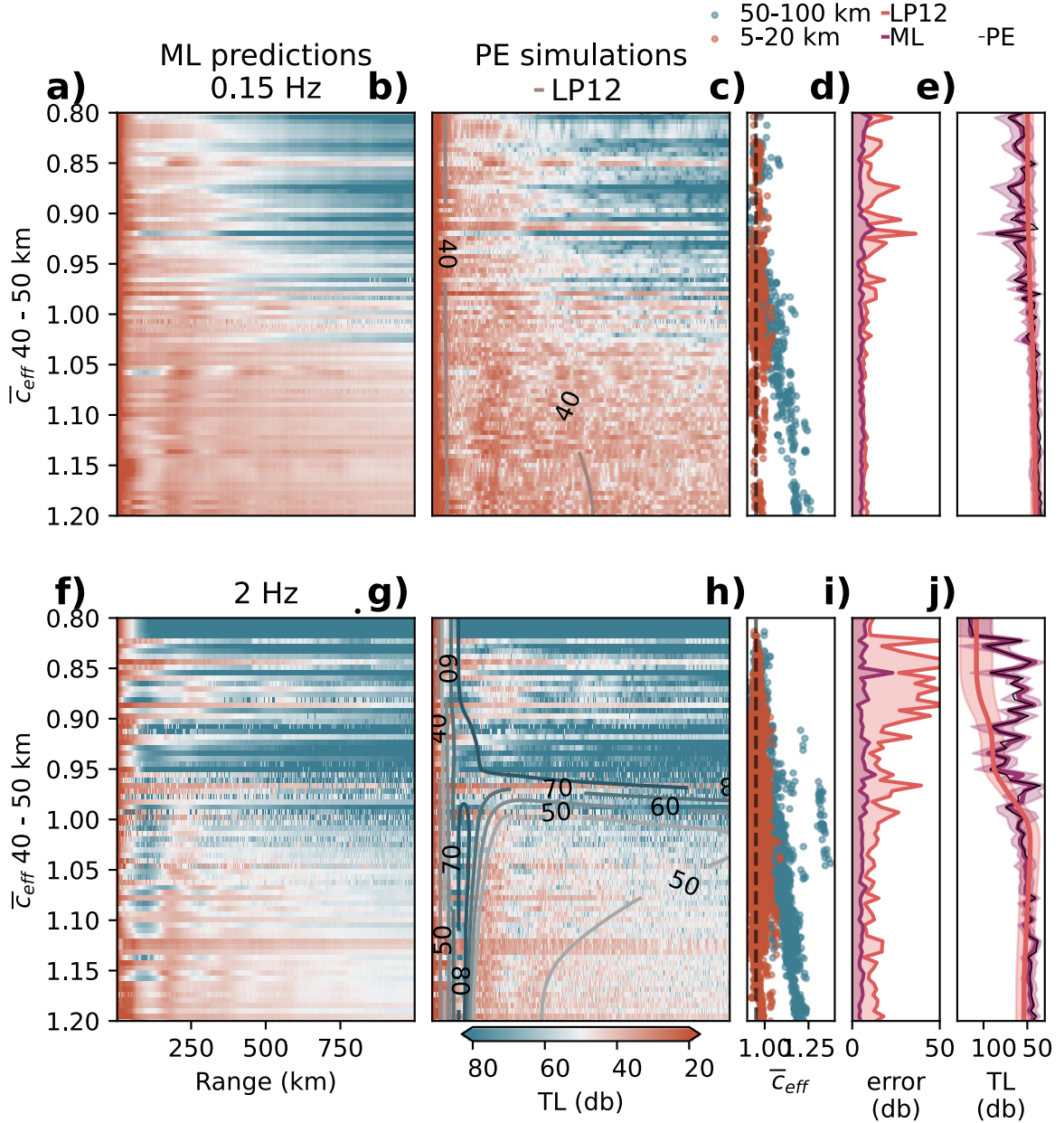


Figure 4. Comparisons of TL maps produced by PE, ML, and LP12 models. (a,b) and (f,g) TL maps vs range and effective velocity ratio \bar{c}_{eff} between 40 – 50 km altitude for a source frequency at 0.15 Hz (a,b) and at 2 Hz (f,g) as predicted by (a,f) the ML model, (b,g) PE simulations, and (b,f isocontours) Le Pichon model. (c,h) effective velocity ratios \bar{c}_{eff} for the troposphere (5 – 20 km altitude, red) and mesosphere-thermosphere (50 – 100 km altitude, blue) at (c) 0.15 Hz (h) and 2 Hz. (d,i) RMSE in dB between the interpolated TL maps from the PE simulations and the ML model (purple) and Le Pichon model (LP12, red) at (d) 0.15 Hz and (i) 2 Hz. (e,j) Median TL in dB vs $\bar{c}_{eff, 40-50 \text{ km}}$ computed from the interpolated TL maps from the PE (black), the ML (purple), and LP12 (red) models at (e) 0.15 Hz and (j) 2 Hz.

272 all values of $\bar{c}_{\text{eff}, 40-50 \text{ km}}$.

273 We also observe that LP12, represented as isocontours in Figs 4b and 4f, is able to capture
 274 the main features of the TL maps, namely the first acoustic shadow zone and first stratospheric
 275 return within 250 km from the source, and the high attenuation for low stratospheric effective
 276 velocity ratios ($\bar{c}_{\text{eff}, 40-50 \text{ km}} < 1$). The good agreement between numerical simulations and
 277 LP12 (Figs 4c and 4h) confirms that average TLs are most sensitive to stratospheric winds
 278 when a strong duct is present. This is also shown in Figs 4e and 4j where we observe that the
 279 high- $\bar{c}_{\text{eff}, 40-50 \text{ km}}$ trends of the median TLs are well captured by LP12. However, Figs 4e and
 280 4j show that errors between the empirical model and PE simulations increase significantly
 281 for low stratospheric effective velocity ratios ($\bar{c}_{\text{eff}, 40-50 \text{ km}} < 1$).

282 LP12 systematically underpredicts the TL for low effective velocity ratios at high frequen-
 283 cies (Fig. 4j), which is consistent with a previous assessment of the empirical model (*Tailpied*
 284 *et al.*, 2021). This owes to the presence of wind ducts outside the stratosphere that are not
 285 accounted for in the empirical model (see Figs 4c and 4g). This is especially true at high
 286 frequencies (*Chunchuzov et al.*, 2015) and close to the source where small wind variations can
 287 make acoustic energy return to the ground (*Chunchuzov et al.*, 2015). Tropospheric ducted
 288 arrivals generally show strong acoustic amplitudes at ground arrays and can represent up to
 289 20% of the energy radiated from the source (*Drob et al.*, 2003). Accounting for tropospheric
 290 ducting is therefore critical for accurate attenuation assessments in the range of distances
 291 from the source ($< 1000 \text{ km}$) considered here. However, these ducts generally exist only up
 292 to a range of $\sim 750 \text{ km}$ and do not affect longer-range propagation at a global scale. Note in
 293 Figs 4c and 4g that there is a bias in our dataset with the presence of thermospheric ducts
 294 only when large stratospheric ducts are present for $\bar{c}_{\text{eff}, 40-50 \text{ km}} > 1$. This bias represents
 295 the inherent correlations present in combined ERA5-NRLMSISE-00 models. Therefore,
 296 considering scenarios with low thermospheric winds and strong stratospheric winds might
 297 lead to a decrease in ML prediction accuracy.

298 6. CONCLUSIONS AND DISCUSSION

299 In this contribution we have proposed an ML-based approach to rapidly ($\sim 0.05 \text{ s}$ runtime)
 300 and reliably ($\sim 5 \text{ dB}$ error on average, compared to PE simulations) predict estimates
 301 of ground TL from surface sources up to 1000 km. The trained ML model takes as input a
 302 range-dependent atmospheric specification and a wave frequency to generate a TL estimate.
 303 Errors compared to full PE simulations remain low for increasing source frequency at close
 304 range of the source. Our ML model can reproduce complex TL where guided tropospheric
 305 waves and multiple stratospheric returns are present. Comparisons with the regression
 306 equation introduced in *Le Pichon et al.* (2012) indicate that considering only the influence
 307 of stratospheric winds between 40 and 50 km altitude enables one to reproduce the main
 308 features of the variations of TL with effective velocity ratio (LP12's errors remain below 10
 309 dB at low frequency for $c_{\text{eff}} > 1$). However, by neglecting the impact of tropospheric and
 310 high-altitude winds, LP12 can lead to significant errors (RMSE $\sim 50 \text{ dB}$) while the ML
 311 model is able to capture accurately the TL for highly heterogeneous wind structures.

312 Several techniques could be used to further improve the accuracy of our ML model.
 313 Running additional simulations will increase the size of the training dataset which will reduce
 314 the RMSE but will not affect the computational cost of ML predictions once trained. Building
 315 on *Raissi et al.* (2019); *Pettit and Wilson* (2020), physical constraints imposed by the PEs
 316 and its boundary conditions could be integrated into the cost function to facilitate the

317 convergence of our ML model. Because we trained our algorithm over atmospheric models
318 extracted only from the ERA5 and the NRLMSISE-00/HWM-14 climatological models,
319 biases might be present in the structure of the input wind fields used for training due to
320 the specific system of equations solved to produce ERA5 models. Acquiring atmospheric
321 models from additional sources (e.g., MERRA dataset as presented in *Kumar et al. (2015)*),
322 could make the ML model more robust to arbitrary wind models. In addition to atmospheric
323 models, small-scale gravity-wave models could be enhanced by considering more realistic
324 range-dependent perturbations (*Drob et al., 2013; Lalande and Waxler, 2016*).

325 Our ML model was trained over a set of simulations generated by a PE modelling tool
326 (*Waxler et al., 2021*) which has strong assumptions about infrasound propagation (see Section
327 2). In particular, PE simulations ignore the influence of cross winds which have a strong
328 impact on the acoustic wavefronts at large distances from the source. ML predictions are
329 expected to be significantly improved if the synthetic dataset were generated using a more
330 accurate modelling tool such as Finite-Differences (FD, *Brissaud et al. (2016); Sabatini*
331 *et al. (2019)*) or Spectral Element Methods (SEM, *Brissaud et al. (2017); Martire et al.*
332 *(2021)*) solving the full linearized Navier-Stokes equations. However, the computational
333 cost associated with such method is much greater than for PE simulations and generating a
334 large synthetic dataset would require extensive computational resources. This cost could be
335 somewhat alleviated since, by resolving the full three-dimensional wavefield, multiple TLs
336 could be extracted from one FD or SEM simulation by considering different azimuths from
337 the source. Once trained over computationally expensive FD or SEM simulations, we can
338 anticipate the cost of one ML simulation to be on the same order than presented here (< 0.1
339 s) which makes ML even more attractive than when trained over PE simulations. In addition
340 to the absence of cross-winds, PE simulations ignore topography which causes a significant
341 scattering of acoustic energy (*Drob et al., 2003*). As FD or SEM tools can incorporate
342 topography, an encoded representation of topographic variations (e.g., one-dimensional
343 CNN) could be concatenated to the frequency and encoded winds to provide more accurate
344 predictions.

345 This work paves the way for the monitoring and characterization of infrasound sources.
346 Recent studies (*Vorobeva et al., 2020; De Carlo et al., 2021*) have shown that infrasound
347 generated by colliding ocean waves, called microbaroms, may provide important constraints
348 on stratospheric winds. To validate their theoretical model connecting ocean sources and
349 observations, these studies rely on the empirical model presented in *Le Pichon et al. (2012)*.
350 Extending the current ML model to longer ranges (> 1000 km) would be useful in, e.g.,
351 global acoustic event analysis, but would also allow an enhanced modelling of microbarom
352 amplitudes, hence also facilitating the development of global infrasound-based near-realtime
353 atmospheric model diagnostics. Crosswinds are not taken into account in PE simulations
354 which would introduce strong uncertainties at greater ranges. The localization of infrasound
355 sources is generally performed using only the arrival times and backazimuth observed at ground
356 arrays and neglects amplitude (e.g., *Blom et al. (2018)*). The absence of amplitude inputs
357 in the optimization process owes to the high computational cost of full-waveform modelling
358 approaches. The inexpensive ML model introduced here could enable the exploration of
359 variations of relative amplitudes between stations with the choice of source location.

360 Finally, because ML models provide an analytical relationship between input wind models
361 and ground TLs, our ML tool could be used to investigate the sensitivity of infrasound
362 amplitudes with variations in wind models. Sensitivity kernels could be built using explanatory
363 techniques such as Layer-wise Relevance Propagation (*Bach et al., 2015*) which propagates

364 the ML predictions backwards in the neural network to determine what part of the input
365 data, i.e., wind model, was used to build a given output, i.e., TL. The construction of
366 wind sensitivity kernels could then be employed to further constrain wind structures in
367 infrasound-based wind inversions (*Vera Rodriguez et al.*, 2020). While we restricted our
368 model to absolute TL predictions, i.e., predictions of the norm of the complex TL, both real
369 and imaginary parts of the TL could be independently predicted. Predicting complex TL
370 would enable one to reconstruct the full infrasound time series from any source time function
371 input (e.g., *Arrowsmith et al.* (2012)).

372 AUTHOR CONTRIBUTIONS

373 Quentin Brissaud (QB) and Sven Peter Näsholm (SPN) initiated this work and elaborated
374 the plan for the study. QB performed the wave propagation simulations and implemented
375 the ML training and validation. Antoine Turquet (AT) implemented the Garder's model in
376 Python. Alexis Le Pichon (ALP) generated the TL profiles using LP12 model (*Le Pichon*
377 *et al.*, 2012) which are presented in Fig. 4. QB created the figures and visualizations, which
378 were further elaborated in collaboration with all co-authors. QB wrote the initial manuscript
379 draft and all co-authors contributed in review, revisions, and editing previous to submission.

380 ACKNOWLEDGMENTS

381 The authors would like to thank Alexander Binder, Associate Professor at the Department
382 of Informatics, University of Oslo, for insightful discussion in the implementation and
383 optimization of Convolutional Neural Networks and transfer learning. The authors are also
384 grateful to Claus Hetzer, Research and Development Engineer at University of Mississippi, for
385 providing details about the theoretical background behind the Parabolic Equations modelling
386 software ePape.

387 This work was mainly funded from a NORSAR institute grant. It was also supported by
388 the project *Middle Atmosphere Dynamics: Exploiting Infrasound Using a Multidisciplinary*
389 *Approach at High Latitudes* (MADEIRA), funded by the Research Council of Norway basic
390 research programme FRIPRO/FRINATEK under Contract No. 274377. This study was
391 facilitated by previous research performed within the framework of the ARISE and ARISE2
392 projects (*Blanc et al.*, 2018, 2019), funded by the European Commission FP7 and Horizon
393 2020 programmes (Grant Nos. 284387 and 653980)

394 DATA AVAILABILITY STATEMENT

395 The ERA5 operational data were accessed from the ECMWF MARS archive using the
396 Climate Data Store API (*ECMWF*, 2018), which is accessible to ECMWF Member and
397 Co-operating States. We are grateful to the National Center for Physical Acoustics (NCPA) at
398 the University of Mississippi for making the Parabolic Equation modelling tool ePape publicly
399 available through GitHub at *Waxler et al.* (2021). The TensorFlow library for Python can be
400 downloaded from the TensorFlow repository (<https://doi.org/10.5281/zenodo.4724125>).
401 The ML model Python implementation, and the corresponding PE TL profiles will be released
402 upon publication on a GitHub repository.

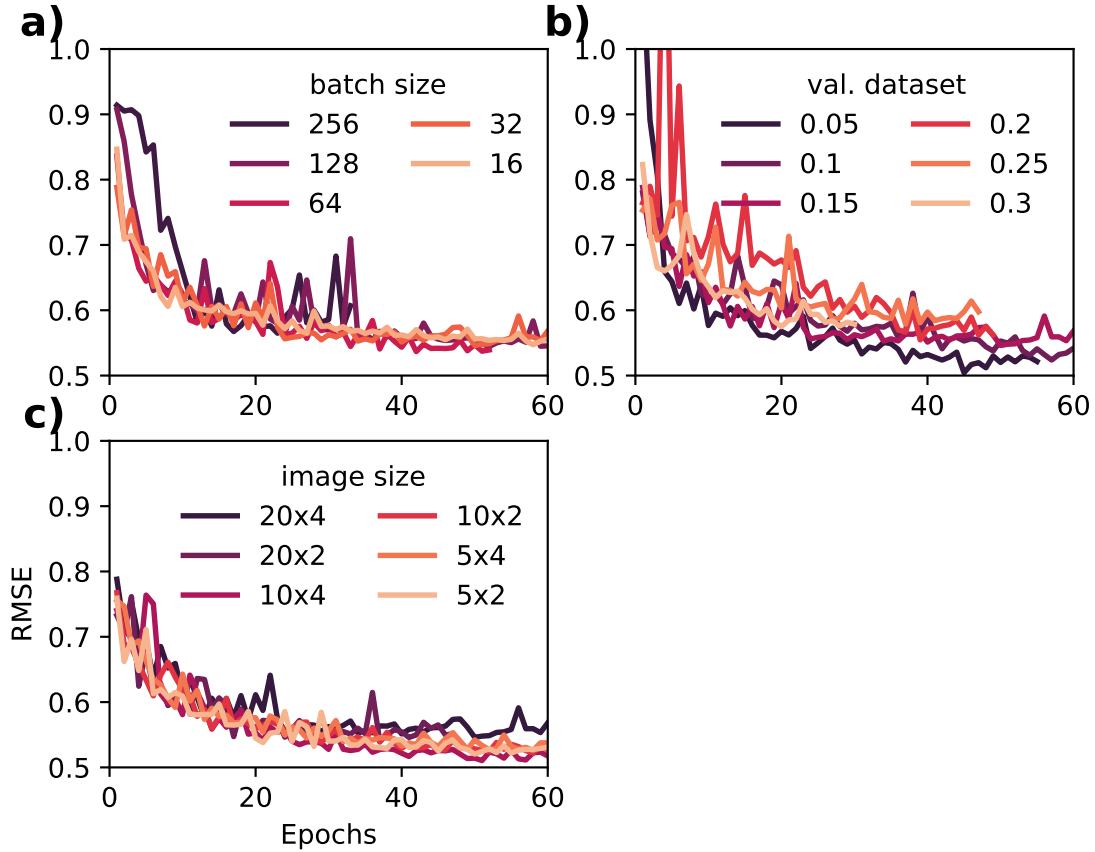


Figure 5. Optimization of training and input hyperparameters. RMSE vs epochs during training for variations in (a) batch size, (b) validation dataset size, and (c) input image size from a baseline model with: batch size 32, 15% validation dataset size, and 20×4 input size.

403 Appendix A: Hyper-parameter optimization

404 The ML model is described by a set of hyper-parameters that must be optimized in order
 405 to obtain the best regression performance. First, we optimized the ML architecture, i.e.,
 406 the number of CNN and dense layers as well as number of CNN filters, using a Bayesian
 407 optimization with Gaussian Processes as implemented in the scikit-optimize Python library
 408 (*Head et al.*, 2021). In addition to architecture optimizations, we investigated the variations
 409 in RMSE with the choice of training parameters (batch size and validation dataset size) as
 410 well as inputs image size. Such variations are shown in Fig. 5. There are generally negligible
 411 error differences between each model. As a trade-off between training time and error we
 412 choose batches of size 32, a dataset of size 20%, and input images of size 20×4 .

413 REFERENCES

414 Abadi, M., A. Agarwal, P. Barham, E. Brevdo, Z. Chen, C. Citro, G. S. Corrado, A. Davis,
 415 J. Dean, M. Devin, S. Ghemawat, I. Goodfellow, A. Harp, G. Irving, M. Isard, Y. Jia,

- 416 R. Jozefowicz, L. Kaiser, M. Kudlur, J. Levenberg, D. Mané, R. Monga, S. Moore,
 417 D. Murray, C. Olah, M. Schuster, J. Shlens, B. Steiner, I. Sutskever, K. Talwar, P. Tucker,
 418 V. Vanhoucke, V. Vasudevan, F. Viégas, O. Vinyals, P. Warden, M. Wattenberg, M. Wicke,
 419 Y. Yu, and X. Zheng (2015), TensorFlow: Large-scale machine learning on heterogeneous
 420 systems, software available from tensorflow.org.
- 421 Arrowsmith, S. J., R. Burlacu, K. Pankow, B. Stump, R. Stead, R. Whitaker, and C. Hayward
 422 (2012), A seismoacoustic study of the 2011 january 3 circleville earthquake, *Geophysical*
 423 *Journal International*, 189(2), 1148–1158, doi:10.1111/j.1365-246X.2012.05420.x.
- 424 Averbuch, G., J. D. Assink, and L. G. Evers (2020), Long-range atmospheric infrasound
 425 propagation from subsurface sources, *J. Acoust. Soc. Am.*, 147(2), 1264–1274, doi:
 426 10.1121/10.0000792.
- 427 Bach, S., A. Binder, G. Montavon, F. Klauschen, K.-R. Müller, and W. Samek (2015), On
 428 pixel-wise explanations for non-linear classifier decisions by layer-wise relevance propagation,
 429 *PloS one*, 10(7), e0130140, doi:10.1371/journal.pone.0130140.
- 430 Blanc, E., L. Ceranna, A. Hauchecorne, A. Charlton-Perez, E. Marchetti, L. Evers, T. Kvaerna,
 431 J. Lastovicka, L. Eliasson, N. Crosby, P. Blanc-Benon, A. Le Pichon, N. Brachet, C. Pilger,
 432 P. Keckhut, J. Assink, P. M. Smets, C. Lee, J. Kero, T. Sindelarova, N. Kämpfer,
 433 R. Rüfenacht, T. Farges, C. Millet, S. Näsholm, S. Gibbons, P. Espy, R. Hibbins, P. Heinrich,
 434 M. Ripepe, S. Khaykin, N. Mze, and J. Chum (2018), Toward an improved representation
 435 of middle atmospheric dynamics thanks to the ARISE project, *Surveys in Geophysics*,
 436 39(2), 171–225, doi:10.1007/s10712-017-9444-0.
- 437 Blanc, E., K. Pol, A. Le Pichon, A. Hauchecorne, P. Keckhut, G. Baumgarten, J. Hildebrand,
 438 J. Höffner, G. Stober, R. Hibbins, P. Espy, M. Rapp, B. Kaifler, L. Ceranna, P. Hupe,
 439 J. Hagen, R. Rüfenacht, N. Kämpfer, and P. Smets (2019), Middle atmosphere variability
 440 and model uncertainties as investigated in the framework of the arise project, in *Infrasound*
 441 *Monitoring for Atmospheric Studies*, pp. 845–887, Springer.
- 442 Blom, P. S., F. K. Dannemann, and O. E. Marcillo (2018), Bayesian characterization
 443 of explosive sources using infrasonic signals, *Geophysical Journal International*, 215(1),
 444 240–251, doi:10.1093/gji/ggy258.
- 445 Brissaud, Q., R. Martin, R. F. Garcia, and D. Komatitsch (2016), Finite-difference numerical
 446 modelling of gravitoacoustic wave propagation in a windy and attenuating atmosphere,
 447 *Geophys. J. Int*, 206(1), 308–327.
- 448 Brissaud, Q., R. Martin, R. F. Garcia, and D. Komatitsch (2017), Hybrid galerkin numerical
 449 modelling of elastodynamics and compressible navier–stokes couplings: applications to
 450 seismo-gravito acoustic waves, *Geophys. J. Int*, 210(2), 1047–1069, doi:10.1093/gji/ggx185.
- 451 Brissaud, Q., S. Krishnamoorthy, J. M. Jackson, D. C. Bowman, A. Komjathy, J. A. Cutts,
 452 Z. Zhan, M. T. Pauken, J. S. Izraelevitz, and G. J. Walsh (2021), The first detection of
 453 an earthquake from a balloon using its acoustic signature, *Geophysical Research Letters*,
 454 48(12), e2021GL093013, doi:10.1029/2021GL093013.
- 455 Chunchuzov, I., and S. Kulichkov (2019), Internal gravity wave perturbations and their
 456 impacts on infrasound propagation in the atmosphere, in *Infrasound Monitoring for*
 457 *Atmospheric Studies*, pp. 551–590, Springer, doi:10.1007/978-3-319-75140-5_16.
- 458 Chunchuzov, I., S. Kulichkov, V. Perepelkin, O. Popov, P. Firstov, J. Assink, and E. Marchetti
 459 (2015), Study of the wind velocity-layered structure in the stratosphere, mesosphere, and
 460 lower thermosphere by using infrasound probing of the atmosphere, *Journal of Geophysical*
 461 *Research: Atmospheres*, 120(17), 8828–8840, doi:10.1002/2015JD023276.

- 462 De Carlo, M., P. Hupe, A. Le Pichon, L. Ceranna, and F. Arduin (2021), Global microbarom
463 patterns: a first confirmation of the theory for source and propagation, *Geophysical Research*
464 *Letters*, *48*(3), e2020GL090163, doi:10.1029/2020GL090163.
- 465 de Groot-Hedlin, C. (2008), Finite-difference time-domain synthesis of infrasound propagation
466 through an absorbing atmosphere, *The Journal of the Acoustical Society of America*, *124*(3),
467 1430–1441, doi:10.1121/1.2959736.
- 468 de Groot-Hedlin, C. D., M. A. Hedlin, and D. P. Drob (2010), Atmospheric variability and
469 infrasound monitoring, in *Infrasound Monitoring for Atmospheric Studies*, pp. 475–507,
470 Springer, doi:10.1007/978-1-4020-9508-5_15.
- 471 Deng, J., W. Dong, R. Socher, L.-J. Li, K. Li, and L. Fei-Fei (2009), Imagenet: A large-scale
472 hierarchical image database, in *2009 IEEE conference on computer vision and pattern*
473 *recognition*, pp. 248–255, Ieee, doi:10.1109/CVPR.2009.5206848.
- 474 Drob, D. P., J. Picone, and M. Garcés (2003), Global morphology of infrasound propagation,
475 *Journal of Geophysical Research: Atmospheres*, *108*(D21), doi:10.1029/2002JD003307.
- 476 Drob, D. P., D. Broutman, M. A. Hedlin, N. W. Winslow, and R. G. Gibson (2013), A
477 method for specifying atmospheric gravity wavefields for long-range infrasound propagation
478 calculations, *Journal of Geophysical Research: Atmospheres*, *118*(10), 3933–3943, doi:
479 <https://doi.org/10.1029/2012JD018077>.
- 480 Drob, D. P., J. T. Emmert, J. W. Meriwether, J. J. Makela, E. Doornbos, M. Conde,
481 G. Hernandez, J. Noto, K. A. Zawdie, S. E. McDonald, J. D. Huba, and J. H. Klenzing
482 (2015), An update to the horizontal wind model (HWM): The quiet time thermosphere,
483 *Earth and Space Science*, *2*(7), 301–319, doi:<https://doi.org/10.1002/2014EA000089>.
- 484 ECMWF (2018), Era5 model level, last accessed on 29 October 2021.
- 485 Evers, L. G., and H. W. Haak (2010), The characteristics of infrasound, its propagation and
486 some early history, in *Infrasound monitoring for atmospheric studies*, pp. 3–27, Springer,
487 doi:10.1007/978-1-4020-9508-5_1.
- 488 Gardner, C. S., C. A. Hostetler, and S. J. Franke (1993), Gravity wave models for the
489 horizontal wave number spectra of atmospheric velocity and density fluctuations, *Journal*
490 *of Geophysical Research: Atmospheres*, *98*(D1), 1035–1049, doi:10.1029/92JD02051.
- 491 Glorot, X., and Y. Bengio (2010), Understanding the difficulty of training deep feedforward
492 neural networks, in *Proceedings of the thirteenth international conference on artificial*
493 *intelligence and statistics*, pp. 249–256, JMLR Workshop and Conference Proceedings.
- 494 Golden, P., P. Negraru, and J. Howard (2012), Infrasound studies for yield estimation of HE
495 explosions, *Tech. rep.*, Southern Methodist University, Dallas Texas.
- 496 Hart, C. R., D. K. Wilson, C. L. Pettit, and E. T. Nykaza (2021), Machine-learning of
497 long-range sound propagation through simulated atmospheric turbulence, *The Journal of*
498 *the Acoustical Society of America*, *149*(6), 4384–4395, doi:10.1121/10.0005280.
- 499 He, K., X. Zhang, S. Ren, and J. Sun (2016), Deep residual learn-
500 ing for image recognition, in *Proceedings of the IEEE conference*
501 *on computer vision and pattern recognition*, pp. 770–778, doi:
502 https://openaccess.thecvf.com/content_cvpr_2016/html/He_Deep_Residual_Learning_CVPR_2016
- 503 Head, T., M. Kumar, H. Nahrstaedt, G. Louppe, and I. Shcherbatyi (2021), scikit-
504 optimize/scikit-optimize, doi:10.5281/zenodo.5565057, last accessed on 29 October 2021.
- 505 Hernandez, B., A. Le Pichon, J. Vergoz, P. Herry, L. Ceranna, C. Pilger, E. Marchetti,
506 M. Ripepe, and R. Bossu (2018), Estimating the ground-motion distribution of the 2016
507 mw 6.2 amatrice, italy, earthquake using remote infrasound observations, *Seismol. Res.*
508 *Lett.*, *89*(6), 2227–2236, doi:10.1785/0220180103.

- 509 Ioffe, S., and C. Szegedy (2015), Batch normalization: Accelerating deep network training
510 by reducing internal covariate shift, in *Proceedings of the 32nd International Conference*
511 *on International Conference on Machine Learning - Volume 37*, ICML'15, p. 448–456,
512 JMLR.org, doi:10.5555/3045118.3045167.
- 513 Kingma, D. P., and J. Ba (2015), Adam: A method for stochastic optimization, in *3rd*
514 *International Conference on Learning Representations, ICLR 2015, San Diego, CA, USA,*
515 *May 7-9, 2015, Conference Track Proceedings*, edited by Y. Bengio and Y. LeCun, doi:
516 arXiv:1412.6980v9.
- 517 Krizhevsky, A., I. Sutskever, and G. E. Hinton (2012), Imagenet classification with deep
518 convolutional neural networks, *Advances in neural information processing systems*, *25*,
519 1097–1105, doi:10.1145/3065386.
- 520 Kumar, G. K., K. K. Kumar, G. Baumgarten, and G. Ramkumar (2015), Validation
521 of MERRA reanalysis upper-level winds over low latitudes with independent rocket
522 sounding data, *Journal of Atmospheric and Solar-Terrestrial Physics*, *123*, 48–54, doi:
523 10.1016/j.jastp.2014.12.001.
- 524 Lai, V. H., Z. Zhan, Q. Brissaud, O. Sandanbata, and M. S. Miller (2021), Inflation
525 and asymmetric collapse at kilauea summit during the 2018 eruption from seismic and
526 infrasound analyses, *Journal of Geophysical Research: Solid Earth*, p. e2021JB022139,
527 doi:10.1029/2021JB022139.
- 528 Lalande, J.-M., and R. Waxler (2016), The interaction between infrasonic waves and gravity
529 wave perturbations: Application to observations using uttr rocket motor fuel elimina-
530 tion events, *Journal of Geophysical Research: Atmospheres*, *121*(10), 5585–5600, doi:
531 <https://doi.org/10.1002/2015JD024527>.
- 532 Le Pichon, A., L. Ceranna, and J. Vergoz (2012), Incorporating numerical modeling into
533 estimates of the detection capability of the ims infrasound network, *Journal of Geophysical*
534 *Research: Atmospheres*, *117*(D5), doi:10.1029/2011JD016670.
- 535 Martire, L., R. Martin, Q. Brissaud, and R. Garcia (2021), Specfem2d-dg, an open source
536 software modeling mechanical waves in coupled solid-fluid systems: the linearised navier-
537 stokes approach, *Geophysical Journal International*, doi:10.1093/gji/ggab308.
- 538 Michalopoulou, Z.-H., P. Gerstoft, B. Kostek, and M. A. Roch (2021), Introduction to the
539 special issue on machine learning in acoustics, *The Journal of the Acoustical Society of*
540 *America*, *150*(4), 3204–3210, doi:10.1121/10.0006783.
- 541 Norris, D., and R. Gibson (2002), Inframap enhancements: environmental/propagation
542 variability and localization accuracy of infrasonic networks, in *Proceedings of the 24th*
543 *Seismic Research Review—Nuclear Explosion Monitoring: Innovation and Integration*, pp.
544 809–813.
- 545 Pettit, C. L., and D. K. Wilson (2020), A physics-informed neural network for sound
546 propagation in the atmospheric boundary layer, in *Proceedings of Meetings on Acoustics*
547 *179ASA*, vol. 42, p. 022002, Acoustical Society of America, doi:10.1121/2.0001383.
- 548 Picone, J., A. Hedin, D. P. Drob, and A. Aikin (2002), NRLMSISE-00 empirical model of the
549 atmosphere: Statistical comparisons and scientific issues, *Journal of Geophysical Research:*
550 *Space Physics*, *107*(A12), SIA–15, doi:10.1029/2002JA009430.
- 551 Raissi, M., P. Perdikaris, and G. E. Karniadakis (2019), Physics-informed neural net-
552 works: A deep learning framework for solving forward and inverse problems involving
553 nonlinear partial differential equations, *Journal of Computational Physics*, *378*, 686–707,
554 doi:10.1016/j.jcp.2018.10.045.

- 555 Sabatini, R., O. Marsden, C. Bailly, and O. Gainville (2019), Three-dimensional direct
556 numerical simulation of infrasound propagation in the earth’s atmosphere, *Journal of Fluid*
557 *Mechanics*, 859, 754–789, doi:10.1017/jfm.2018.816.
- 558 Shani-Kadmiel, S., G. Averbuch, P. Smets, J. Assink, and L. Evers (2021), The 2010 haiti
559 earthquake revisited: An acoustic intensity map from remote atmospheric infrasound obser-
560 vations, *Earth and Planetary Science Letters*, 560, 116,795, doi:10.1016/j.epsl.2021.116795.
- 561 Simonyan, K., and A. Zisserman (2015), Very deep convolutional networks for large-scale
562 image recognition, in *3rd International Conference on Learning Representations, ICLR*
563 *2015, San Diego, CA, USA, May 7-9, 2015, Conference Track Proceedings*, edited by
564 Y. Bengio and Y. LeCun.
- 565 Sutherland, L. C., and H. E. Bass (2004), Atmospheric absorption in the atmosphere
566 up to 160 km, *The Journal of the Acoustical Society of America*, 115(3), 1012–1032,
567 doi:10.1029/2006JD007806.
- 568 Tailpied, D., A. L. Pichon, and B. Taisne (2021), Assessing uncertainties in infrasound
569 network performance modelling: application to the Euro-Mediterranean and Southeast
570 Asian region, *Geophysical Journal International*, doi:10.1093/gji/ggab399, ggab399.
- 571 Vera Rodriguez, I., S. P. Näsholm, and A. Le Pichon (2020), Atmospheric wind and
572 temperature profiles inversion using infrasound: an ensemble model context, *J. Acoust.*
573 *Soc. Am.*, 148(5), 2923–2934, doi:10.1121/10.0002482.
- 574 Vorobeva, E. E., M. D. Carlo, A. L. Pichon, P. J. Espy, and S. P. Näsholm (2020),
575 Microbarom radiation and propagation model assessment using infrasound recordings: a
576 vespagram-based approach, *Annales Geophysicae*, pp. 1–22, doi:10.5194/angeo-2020-78.
- 577 Waxler, R., C. Hetzer, J. Assink, and D. Velea (2021), chetzer-ncpa/ncpaprop-release:
578 Ncpaprop v2.1.0, doi:10.5281/zenodo.5562713, last accessed on 29 October 2021.